catalysts

MDPI

Article

Fabrication of TiO_2-WO_3 S-Scheme Heterojunction for High-Efficiency Visible-Light Photocatalysis

Yang Deng [1], Shuhong Wu [2,*] and Jun Zhu [1,2,3,*]

[1] School of Materials Science and Engineering, Shanghai Jiao Tong University, Shanghai 200240, China; yang.d@sjtu.edu.cn
[2] National Engineering Research Center for Nanotechnology, 28 East Jiang Chuan Road, Shanghai 200241, China
[3] SJTU Asia-Pacific Graduate Institute (SJTU-APGI), 1 Create Way, #14-01 CREATE Tower, Singapore 138602, Singapore
* Correspondence: wushuhong0924@163.com (S.W.); yzjzhu@163.com (J.Z.)

Abstract

Driven by the progress of sustainable development, environmental remediation and water treatment have become increasingly important. Photocatalysis, capable of degrading pollutants through light (especially visible light) irradiation, has received widespread research attention. Titanium dioxide(TiO_2) is a promising photocatalyst, yet its practical use is limited by low visible-light utilization and rapid photogenerated charge recombination. Herein, an S-scheme TiO_2-WO_3(Tungsten trioxide) heterojunction was successfully fabricated; the difference in Fermi levels induces a built-in electric field directed from TiO_2 to WO_3, which thus constructs the S-scheme heterojunction. The as-prepared heterojunction exhibits a markedly enhanced transient photocurrent density, with the carrier lifetime prolonged from 2.69 ns to 41.61 ns. Under visible-light irradiation, the heterojunction achieves a methylene blue (MB) removal efficiency of over 95% within 90 min, and its pseudo-first-order kinetic rate constant k reaches 0.032 min^{-1}, which is approximately 16 times that of pure TiO_2. Radical trapping experiments confirm that the dominant active species responsible for the catalytic process are photogenerated holes and the hydroxyl radicals derived therefrom.

Keywords: photocatalysis; TiO_2/WO_3 heterojunction; band structure engineering

1. Introduction

With rapid technological advancement, water pollution poses a serious threat to ecosystems and human health, making efficient remediation urgently needed. MB, a toxic and persistent dye commonly present in industrial wastewater, is difficult to degrade even at low concentrations. Photocatalysis has emerged as a sustainable and environmentally friendly strategy for pollutant removal. Since the pioneering work of Honda and Fujishima on TiO_2 photocatalysis [1], TiO_2 has been widely investigated due to its high stability, strong oxidation ability, and natural abundance [2,3]. However, its wide band gap (3.0–3.2 eV) and rapid charge carrier recombination severely limit visible-light utilization and photocatalytic efficiency [4]. Consequently, various modification strategies, such as doping, heterojunction construction, noble metal loading, and defect engineering, have been developed to enhance charge separation and photocatalytic performance [5–9].

Constructing heterojunctions has been widely recognized as an effective strategy to promote the separation of photogenerated charge carriers and suppress their recombi-

Check for updates

Academic Editor: Jorge Bedia

Received: 24 January 2026
Revised: 18 March 2026
Accepted: 18 March 2026
Published: 10 April 2026

Copyright: © 2026 by the authors. Licensee MDPI, Basel, Switzerland. This article is an open access article distributed under the terms and conditions of the Creative Commons Attribution (CC BY) license.

nation, thereby enhancing photocatalytic performance [10]. Beyond charge separation efficiency, increasing attention has been paid to the intrinsic redox potentials of charge carriers, which are closely related to band structure characteristics [11,12]. Generally, wide-band-gap semiconductors exhibit strong redox capability but limited light absorption, whereas narrow-band-gap materials enable broader light harvesting at the expense of redox power [12]. Rationally designed heterojunctions with tailored band-edge alignment offer an effective solution to this intrinsic trade-off [13]. Among various heterojunction architectures, the S-scheme heterojunction proposed by Jiaguo Yu et al. in 2019 is considered one of the most rational and efficient configurations for photocatalysis [14]. Numerous studies have validated its superiority in maintaining strong redox ability while achieving efficient charge separation. For instance, S-scheme systems such as carbon nitride/CdSe [15], TiO_2/Bi_2O_3 [16], In_2O_3@TiO_2 [17], $BiVO_4/TiO_2$ [18], g-C_3N_4/TiO_2 [19] and TiO_2/Bi_2WO_6 [20] have demonstrated dramatically enhanced photocatalytic activities in pollutant degradation, H_2O_2 production, and photocatalytic H_2 evolution, respectively, compared with their individual components.

In conclusion, WO_3 is a unique oxide that enhances the functional properties of many materials, making it suitable for a wide range of applications as a typical n-type semiconductor [21,22]. Numerous studies have demonstrated that oxidative degradation is an effective approach for removing organic pollutants from wastewater [23,24], and WO_3 has been widely employed in various modified photocatalytic systems, such as WO_3/In_2S_3 [8], WO_3/TiO_2/rGO [25], $WO_3/Cu/WO_3$ [26], and $ZnIn_2S_4/WO_3$ [27]. However, the charge transfer pathways and photocatalytic mechanisms in many reported systems have not been fully elucidated. Therefore, in this work, WO_3 is selected to construct an S-scheme heterojunction photocatalyst with TiO_2, which is expected to exhibit superior photocatalytic performance owing to its rationally designed heterojunction architecture. The photocatalytic degradation of methylene blue under visible-light irradiation is systematically investigated, and the corresponding degradation pathway and underlying photocatalytic mechanism of the TiO_2/WO_3 nanocomposite are further elucidated.

2. Results and Discussion

2.1. Crystal Structure and Morphology

The preparation process of the TiO_2-xW composite is illustrated in Figure 1a. Initially, TiO_2-0 was synthesized via a hydrothermal method using $TiCl_4$ as the precursor. The XRD result of TiO_2-0 (Figure S1) shows that the crystal structure of TiO_2-0 matches PDF#74-1940, and SEM images of TiO_2-0, TiO_2, and TiO_2-650 (Figure S2) reveal that all samples consist of uniform nanoparticles approximately 200 nm in size. Furthermore, with an increase in calcination temperature, the particle surface becomes progressively smoother, resulting in a decrease in specific surface area. While this effect is not pronounced at 350 °C, it becomes markedly evident at 650 °C (Figure S2). FT-IR spectroscopy (Figure S3) further reveals that the surface of TiO_2-0 contains numerous organic groups, which can be effectively removed by calcination, so calcination is crucial to eliminate the surface transition layer, thereby enhancing carrier transfer across the interface. Subsequently, H_2WO_4 was deposited on TiO_2-0 using $Na_2WO_4 \cdot 2H_2O$ as a tungsten source, followed by calcination at 350 °C for 4 h to decompose H_2WO_4 into WO_3, forming TiO_2/WO_3 composite. Combined with the detailed micrograph images of TiO_2-0 and TiO_2 in Figures S4 and S5, it is suggested that calcination at 350 °C effectively removes the surface groups while preserving the initial morphology of the sample.

XRD and Raman spectroscopy were conducted on samples before and after WO_3 loading (Figure 1b,c). As shown in Figure 1b, all samples exhibit three distinct diffraction peaks at 25.2°, 36.9° and 48.0°, indexed to the (101), (103), and (200) planes of anatase TiO_2

(reference PDF#21-1272) [28], confirming the anatase as the main component of the TiO_2 matrix (Figure S6), which owns stable and efficient photocatalytic activity [29]. In addition, a diffraction peak at around 27° (corresponding to (111) and (102) planes of monoclinic WO_3) appears in Figure 1b, and its intensity is increased with the loading amount of WO_3, indicating the successful incorporation and enrichment of WO_3. The Raman spectra of TiO_2-xW (Figure 1c) display peaks at 146.2 cm^{-1}, 199.3 cm^{-1}, 256.9 cm^{-1}, 515 cm^{-1}, and 639 cm^{-1}, which are characteristic of the Eg vibrational modes of anatase. Notably, a peak at 256.9 cm^{-1}, which does not correspond to any TiO_2 polymorph, is observed in the WO_3-loaded samples, attributed to W-O-W bending vibrations [27], in agreement with the XRD results.

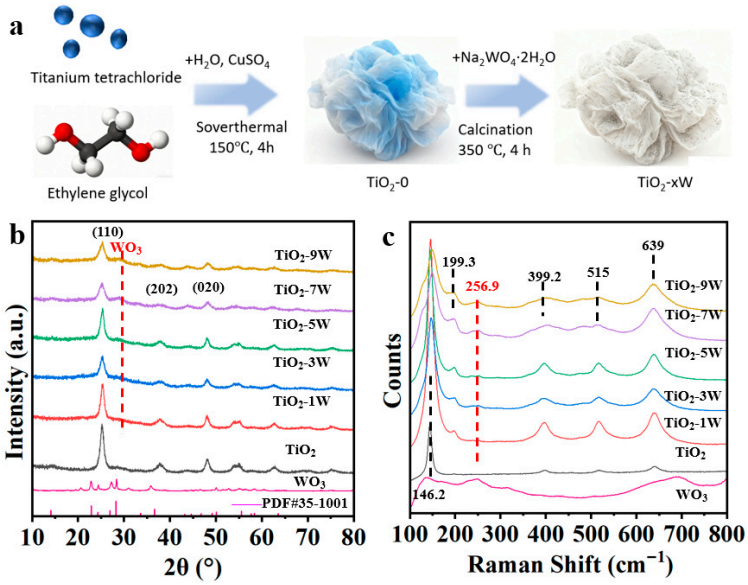


Figure 1. (**a**) Schematic illustration of the preparation process of the TiO_2-5W sample; (**b**) XRD results of different samples; (**c**) Raman spectra of different samples.

SEM and TEM images of TiO_2-5W (Figure 2) reveal that TiO_2 forms spherical clusters composed of ultrathin nanosheets, a microstructure that enhances the specific surface area and provides abundant active sites to improve photocatalytic performance. WO_3 loading made the surface smoother with reduced porosity as WO_3 fills the intrinsic pores of TiO_2. For comparison, pristine WO_3 (synthesized via sodium tungstate precipitation) showed severe agglomeration (Figure S7), while TiO_2-5W had no distinct WO_3 morphology or agglomeration. This phenomenon is related to the material preparation method. WO_3 particles precipitated directly from the solution lack effective anchoring sites and thus tend to aggregate. In contrast, when TiO_2 powder is introduced into the solution system, WO_3 preferentially deposits onto the TiO_2 surface, which reduces the aggregation effect. Combined with the EDS mapping (Figure S8) result, it is clear that the distribution of W and Ti is uniform, confirming the homogeneous dispersion of WO_3 within the TiO_2 matrix and the formation of a robust heterostructure. In addition, EDS quantitative analysis shows Ti, O, W, and trace Cu in TiO_2-5W, and the W mass fraction is 2.59%, consistent with the theoretical 2.7%, further verifying successful WO_3 loading. The purpose of doping with Cu here is to introduce defects and thereby enhance the response of the TiO_2 matrix to visible light [28]. HRTEM images (Figure 2d) show distinct lattice fringes with an interplanar spacing of 0.352 nm, corresponding to the anatase TiO_2 (101) plane. Additional fringes in Figure 2d match the WO_3 (301) and (200) planes. The dashed line in Figure 2d highlights the TiO_2/WO_3 interface, providing direct evidence of heterostructure formation. No obvious surface transition layer is observed, suggesting direct lattice matching, which facilitates

the rapid transfer and separation of photogenerated charge carriers and is a key factor for efficient photocatalysis.

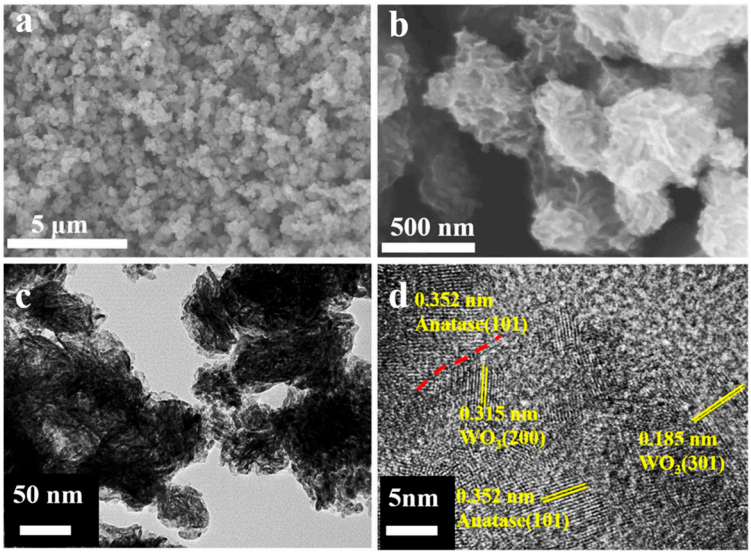


Figure 2. (**a**,**b**) SEM images of TiO_2-5W; (**c**,**d**) TEM and HRTEM images of TiO_2-5W.

Furthermore, as shown in Figure S9 (BET results) and Table S1 (analytical data), both TiO_2 and TiO_2-5W exhibit typical Type IV isotherms with H_1-type hysteresis loops in the relative pressure (P/P_0) range of 0.3–1.0. The H_1 hysteresis indicates mesoporous structures with uniform pore size [30] and is associated with effects such as pore channel narrowing or cylindrical pore blocking [31]. Table S1 shows that the specific surface areas of TiO_2 and TiO_2-5W are 118.08 m^2/g and 129.79 m^2/g, respectively; BJH analysis gives average pore sizes of 11.586 nm and 9.493 nm, and pore volumes of 0.385 cm^3/g and 0.308 cm^3/g. Compared to TiO_2, TiO_2-5W exhibits reduced pore size and volume, a result attributed to the uniform loading of WO_3 that fills the TiO_2 pores, as confirmed by previous microstructural analyses. However, the presence of the W precursor on TiO_2 suppresses sintering during calcination, leading to a slight increase in the specific surface area. Consequently, moderate WO_3 loading can effectively enhance the specific surface area of TiO_2.

2.2. XPS Results

Based on the previous analysis, WO_3 can be effectively loaded onto the TiO_2 surface via calcination, enabling the successful fabrication of the TiO_2/WO_3 hetero composite. To further characterize the surface element composition and electron interactions between the two semiconductors, XPS was employed to analyze the as-prepared heterojunction samples, with the results presented in Figure 3. As shown in the full-scan XPS spectrum (Figure 3a), the TiO_2-5W heterojunction sample contains Ti, O, and W elements, confirming that TiO_2-5W is a TiO_2/WO_3 composite. In addition, no peak corresponding to Cu 2p is observed in the full-scan spectrum, which can be attributed to the low Cu doping level and the fact that Cu elements are located in the lattice of TiO_2 rather than on the surface, making them undetectable. Figure 3b displays the high-resolution XPS spectrum of the Ti 2p peak. It can be seen that the high-resolution Ti 2p spectrum of the pristine TiO_2 matrix consists of two main peaks at binding energies of 458.53 eV ($2p_{3/2}$) and 464.21 eV ($2p_{1/2}$), along with a satellite peak at approximately 471.47 eV. The XPS spectra of the heterojunction sample loaded with WO_3 also contain these three peaks, while the Ti $2p_{3/2}$ peak of TiO_2-5W shifts to higher binding energy by approximately 0.2 eV compared with that of TiO_2. This phenomenon can be attributed to electron transfer from TiO_2 to WO_3,

which reduces the electron density of Ti and consequently, increases the binding energy of Ti. This suggests charge transfer occurring at the interface between the two semiconductors, which is crucial for the photocatalytic process. A similar shift phenomenon is observed in the high-resolution O 1s spectrum in Figure 3c. Compared with TiO_2, the binding energy of lattice oxygen in the TiO_2-5W shifts to lower binding energy. The peak at a binding energy of approximately 531.59 eV in both samples is assigned to adsorbed oxygen (O_A) [32,33], and the two materials show nearly identical binding energy for this O_A peak. Furthermore, quantitative analysis of the peak areas in the high-resolution O 1s spectrum indicates that the relative proportion of the O_A peak area is increased in TiO_2-5W. This suggests that WO_3 loading increases the proportion of O_A, thereby enhancing the number of adsorption sites to some extent. In the high-resolution W 4f spectrum of Figure 3d, two peaks are detected with the binding energies of 35.29 eV and 37.13 eV, which correspond to the $4f_{7/2}$ and $4f_{5/2}$ peaks of W^{6+} ions [30,34], respectively. No peaks corresponding to W^{5+} ions are observed, indicating that W in the sample exists in the form of WO_3. Therefore, the XPS analysis results further confirm the presence of charge transfer between TiO_2 and WO_3 during the preparation process of the TiO_2-5W, which is, TiO_2 transfers negative charges to WO_3. This charge transfer process results in the formation of a heterojunction between the two components, facilitating the separation and transfer of photogenerated charge carriers, thus enhancing photocatalytic activity.

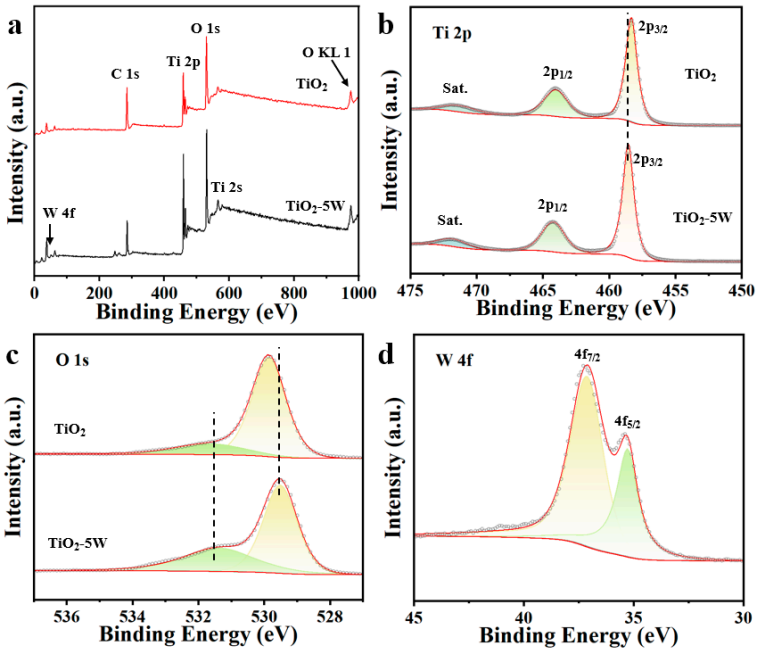


Figure 3. XPS spectra: (**a**) Survey scan; (**b**) High-resolution Ti 2p spectrum; (**c**) High-resolution O 1s spectrum; (**d**) High-resolution W 4f spectrum of TiO_2-5W. The red curve represents the fitted curve, while the scatter points represent the raw data.

2.3. Optical Properties and S Scheme Heterojunction Analysis

The band gap of semiconductors directly determines their visible-light absorption capacity, which is critical for photocatalytic performance. Thus, UV-vis absorption spectroscopy and Mott–Schottky (M-S) measurements were performed to systematically characterize the band structures of as-prepared samples. UV-vis absorption spectra in Figure 4a show that all samples exhibit strong absorption in the 200–400 nm UV region. The absorption edge of WO_3 is around 460 nm, while those of TiO_2 and TiO_2-5W are approximately 380 nm. Notably, TiO_2-5W exhibits slightly enhanced visible-light absorption compared to pristine TiO_2, which is attributed to the formation of TiO_2-WO_3 heterojunction, while it

is relatively weak due to the amount of WO_3 loading. Band gap values were derived via linear extrapolation of Tauc plots (Figure S10). For direct band gap WO_3 (Tauc plot ordinate set as $(\alpha h\upsilon)^2$) [35], the calculated band gap is 3.04 eV, slightly higher than the literature values [36], due to residual crystal water in WO_3 from incomplete H_2WO_3 decomposition during synthesis. The band gap of TiO_2-5W heterojunction is 2.89 eV, lower than that of pristine TiO_2 (2.97 eV). This reduction is attributed to the formation of the TiO_2/WO_3 heterojunction, which modulates the visible-light response of TiO_2, although the effect is limited by the low WO_3 content.

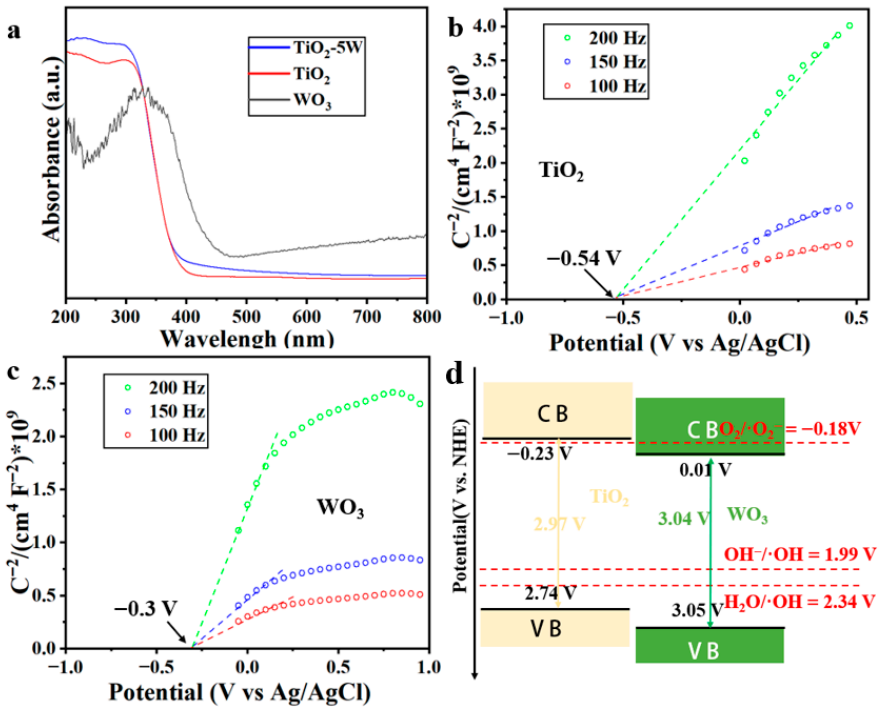


Figure 4. (**a**) UV-vis absorption spectra of the samples; Mott–Schottky tests of (**b**) TiO_2 and (**c**) WO_3; (**d**) Schematic of the band edge positions of the two semiconductors.

M-S measurements were conducted to determine semiconductor types and flat-band potentials of the heterojunction components. The positive slopes of M-S plots (Figure 4b,c) confirm that both TiO_2 and WO_3 are n-type semiconductors. Extrapolating linear segments gives their flat-band potentials relative to Ag/AgCl as –0.54 V (TiO_2) and –0.30 V (WO_3). The conversion of a reversible hydrogen electrode to NHE (pH = 0) gives values of 0.07 V and 0.31 V; the specific conversion formula details are shown in Formula S1 in the Supporting Information [37]. Given the low doping levels, the flat-band potential of n-type semiconductors approximates their Fermi lever [38], and the conductor band is 0.1–0.3 V higher than the Fermi lever [17,39], so the conductor band minimums of TiO_2 and WO_3 are estimated to be –0.23 V and 0.01 V. Combined with calculated band gaps, the band structure (Figure 4d) shows a staggered alignment of TiO_2 and WO_3 energy bands: both CB and valence band (VB) edges of WO_3 are more positive than TiO_2, forming an S-scheme heterojunction that facilitates charge carrier separation and migration.

Apart from the band gaps and the position of the edge of CB and VB of different semiconductors, the built-in electric field (IEF) is another crucial factor to understand the mechanism of S-scheme heterojunction, while Fermi level is the critical parameter to analyze the formation process of IEF. Numerous studies [40,41] have confirmed that the anatase TiO_2 (001) facet is the most reactive. Thus, theoretical calculations were performed to determine the work functions (W) of the TiO_2 (001) and WO_3 (001) facets, and the structural models of TiO_2 and WO_3 are shown in Figure S11, with results shown in Figure 5a,b.

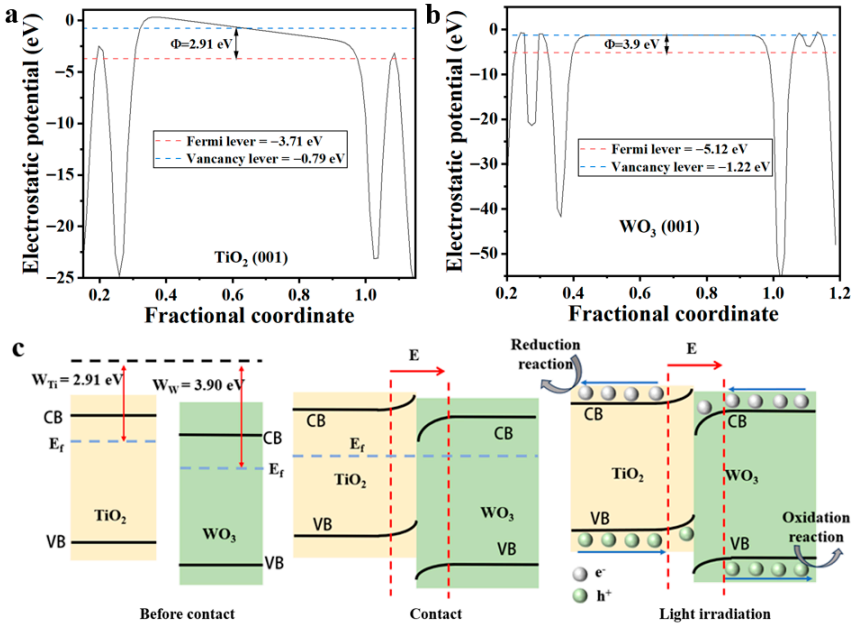


Figure 5. Diagrams related to Fermi levels of TiO_2 and WO_3 and heterojunction formation mechanism: theoretical calculation results of work functions for (**a**) TiO_2 (001) facet and (**b**) WO_3 (001) facet; (**c**) Schematic diagram of electron transfer, band bending, and built-in electric field (IEF) construction during the formation of TiO_2/WO_3 heterojunction.

It is evident from Figure 5a,b that the theoretically derived work functions are 2.91 eV for TiO_2 (001) and 3.90 eV for WO_3 (001), the values are slightly different from those reported in previous studies, but the difference in work function between the TiO_2 (001) and WO_3 (001) surfaces remains similar, at approximately 1.0 eV [42,43], with corresponding vacuum energy levels (Vac, used as references) of −0.79 eV and −1.22 eV, respectively. Based on the formula $E_f = V_{ac} - W$ (where V_{ac} is vacuum energy level, E_f = Fermi level), the Fermi levels of TiO_2 and WO_3 are calculated as −3.71 eV and −5.12 eV, respectively. Notably, the Fermi level of TiO_2 is higher than WO_3. During the process of contact, the Fermi level difference drives electron transfer from TiO_2 to WO_3 across the interface until Fermi level equilibrium is achieved. This process induces interfacial band bending of both semiconductors: TiO_2 loses electrons and becomes positively charged at the interface, while WO_3 gains electrons and becomes negatively charged. Consequently, an IEF directed from TiO_2 to WO_3 is formed at the interface. Owing to the energy distribution of negatively charged electrons, the electron potential energy increases along the electric field direction, leading to upward band bending of TiO_2 and downward band bending of WO_3, forming the S-scheme heterojunction (Figure 5c). Under light irradiation, the IEF promotes the migration of photogenerated holes in TiO_2 and photogenerated electrons in WO_3 to the interface, facilitating their recombination. In contrast, photogenerated electrons in TiO_2 and photogenerated holes in WO_3 cannot cross the interface due to the IEF barrier. Thus, photogenerated electrons with a higher band edge position (in TiO_2) and photogenerated holes with a lower band edge position (in WO_3) are physically separated, effectively suppressing carrier recombination [12]. Additionally, the edge position of the energy band is closely associated with the redox capability of carriers: holes at lower VB positions exhibit stronger oxidizing ability, while electrons at higher CB positions possess stronger reducing ability [38]. Therefore, the holes in the TiO_2/WO_3 heterojunction have a stronger oxidizing capacity than those in TiO_2, which can significantly enhance its aquatic pollutant removal efficiency [27]. Based on these analyses, it can be predicted that the heterojunction will exhibit superior electron transport and transfer capabilities, and thus demonstrate high efficiency in the photocatalytic degradation of pollutants.

2.4. Charge Separation and Photocatalyst Activity

Numerous studies have demonstrated that the photogenerated carrier separation efficiency of materials is a crucial factor determining the carrier concentration [5,10,44–46], as efficient carrier separation can enhance the proportion of carriers available for participation in photocatalytic reactions. According to the aforementioned analysis, TiO_2 and WO_3 form an S-scheme heterojunction, which theoretically improves the migration and separation efficiency of photogenerated carriers. To verify the effectiveness of this heterojunction, transient photocurrent (i-t curve) measurements and electrochemical impedance spectroscopy (EIS) tests were conducted on the as-prepared TiO_2, WO_3, and composite TiO_2-5W samples to assess their photogenerated carrier separation and transfer capabilities.

Figure 6a presents the transient photocurrent curves of the samples. It can be observed that the pristine TiO_2 and WO_3 exhibit relatively low photocurrents: the maximum photocurrent of TiO_2 is approximately 0.05 $\mu A/cm^2$, while that of WO_3 is about 0.03 $\mu A/cm^2$. In contrast, the photocurrent of the composite TiO_2-5W heterojunction is significantly enhanced to approximately 0.33 $\mu A/cm^2$. The remarkable increase in photocurrent density indicates a higher carrier concentration in the heterojunction sample, allowing more carriers to migrate to the sample surface and participate in catalytic reactions. Figure 6b illustrates the EIS Nyquist plots of different samples. The TiO_2-5W sample exhibits the smallest radius of the semicircular arc in its EIS plots, indicating a high electron transfer rate. This facilitates the separation of photogenerated carriers [5,47] and thus can effectively improve the photocatalytic performance of the material. In the PL spectroscopy results shown in Figure 6c, the heterojunctions loaded with WO_3 display a significant reduction in fluorescence intensity; this also demonstrates that the construction of heterojunctions improves the separation efficiency of photogenerated electrons and holes, while greatly suppressing carrier recombination. Furthermore, the PL spectra of WO_3 and TiO_2-5W exhibit similar peaks, suggesting that charge carrier recombination in TiO_2-5W mainly occurs in WO_3, indicating that WO_3 acts as the recombination center. In addition, the time-resolved photoluminescence (TRPL) spectra of the samples shown in Figure 6d were fitted using a triple exponential function, i.e., the experimental curves were considered to satisfy the following Equation (1):

$$R(t) = B_1 e^{(-t/\tau_1)} + B_2 e^{(-t/\tau_2)} + B_3 e^{(-t/\tau_3)}, \quad (1)$$

where B_1, B_2 and B_3 are the pre-exponential factors corresponding to τ_1, τ_2 and τ_3, respectively, and τ_1, τ_2 and τ_3 represent the decay times of each decay component. The relevant data obtained after fitting are presented in Table S2.

The average decay times can be represented by the following Equation (2):

$$\tau = (B_1\tau_1^2 + B_2\tau_2^2 + B_3\tau_3^2)/(B_1\tau_1 + B_2\tau_2 + B_3\tau_3), \quad (2)$$

Calculations indicate that the decay time of TiO_2 is 2.69 ns and the decay time of WO_3 1.49 ns, while that of the TiO_2-5W is 41.61 ns, which is much longer than that of both pristine TiO_2 and WO_3. It is evident that WO_3 loading can significantly improve the carrier separation efficiency and remarkably extend the carrier lifetime of the pristine TiO_2 matrix. This result is consistent with the data from transient photocurrent and PL spectra, confirming that the formation of S-scheme TiO_2/WO_3 heterojunction can effectively promote the separation efficiency of charges and reduce the carrier recombination rate, ensuring more carriers migrate to the catalyst surface to participate in catalytic reactions.

The results of the photocatalytic experiments are presented in Figure 7. The reaction system was placed in the dark for 60 min to achieve adsorption–desorption equilibrium. As shown in Figure 7a, the initial degradation concentrations of different samples varied,

which is attributed to the differences in the adsorption capacities of various samples for MB. It can be seen from Figure 7c that with the increase in WO_3 loading, the adsorption capacity of the samples for MB increased. Within this loading range, WO_3 loading can significantly enhance the MB adsorption capacity of pristine TiO_2. In addition, we performed photocatalytic degradation experiments of methylene blue using TiO_2-5W under different pH conditions, and the results are shown in Figure S12. It can be seen that the adsorption capacity of TiO_2-5W for methylene blue varies significantly with pH, indicating that the surface charge and functional group distribution of the sample affect the adsorption of MB and thus its photocatalytic performance. Therefore, we attribute the change in adsorption capacity shown in the figure mainly to the surface charge variation and hydroxyl group formation of TiO_2 induced by WO_3 loading [48]. After turning on the xenon lamp irradiation, the photocatalytic reaction process can be described by the pseudo-first-order kinetic model [24,47,49,50], i.e., the concentration c of the sample satisfies Equation (3):

$$-\ln\left(\frac{C}{C_0}\right) = kt, \tag{3}$$

where C is the sample concentration, C_0 is the initial concentration, k is the photocatalytic degradation rate constant, and t is the reaction time. As shown in the plot of $-\ln(C/C_0)$ versus time t (Figure 7b), TiO_2-5W exhibits the largest slope, indicating the highest photocatalytic reaction rate among all samples. Additionally, the bar chart of k values (Figure 7c) reveals that within a certain range, the reaction rate constant k increases with increasing W content. The TiO_2-5W sample achieves a maximum rate constant of 0.03216 min^{-1}, with a MB removal rate exceeding 95% after 90 min of irradiation, making it the optimal photocatalytic material. To demonstrate the superiority of the performance of our samples, we have summarized the photocatalytic performance of several TiO_2-related catalysts in Table S3. It can be seen from the table that the photocatalytic performance of the as-prepared S-scheme heterojunction is superior. However, a further increase in W content results in a decrease in the reaction rate constant.

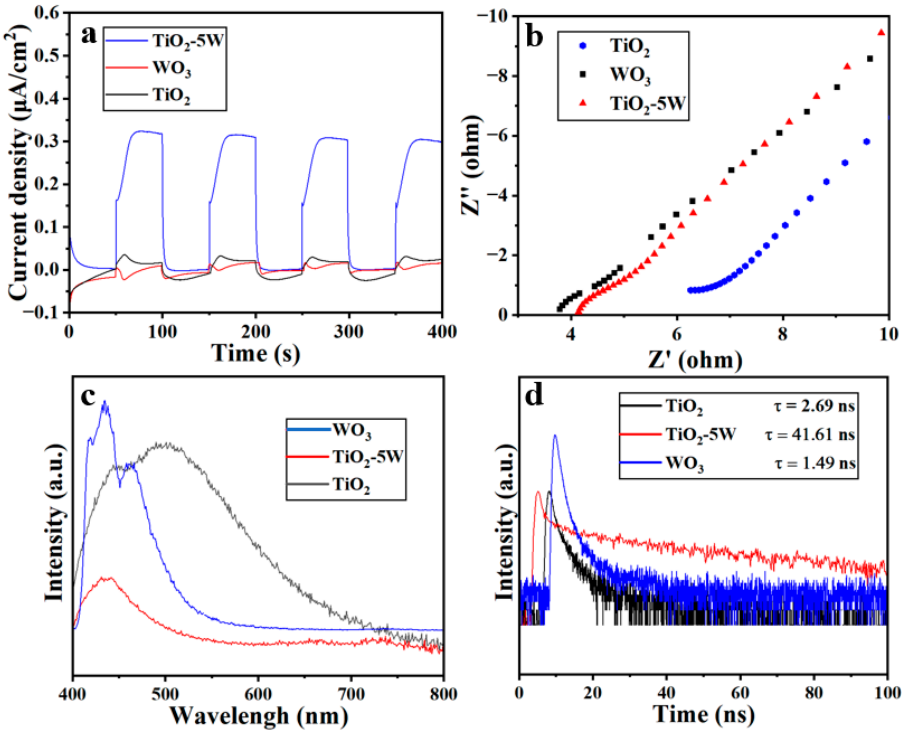


Figure 6. Electrochemical and fluorescence measurement results: (**a**) i-t curve; (**b**) EIS; (**c**) PL spectrum; (**d**) TRPL results.

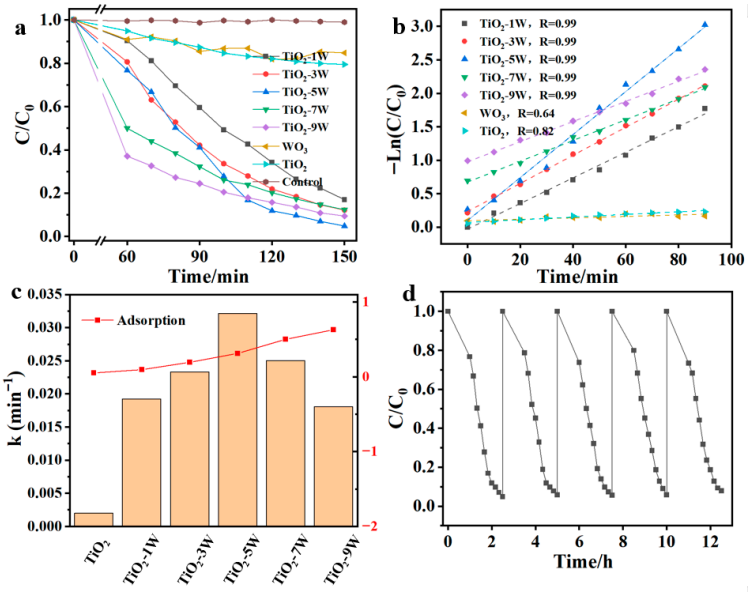


Figure 7. Photocatalytic Performance: (**a**) Degradation curves; (**b**) Pseudo-first-order kinetic fitting curves; (**c**) Adsorption capacities of the samples derived from (**a**) and slopes of the fitted curves obtained from (**b**); (**d**) Cycling test of TiO_2-5W.

This phenomenon can be explained as follows: the loading of WO_3 successfully constructs the S-scheme heterojunction, which slightly enhances the visible-light response of the sample, effectively promotes the migration and separation of photogenerated carriers, and retains the holes with stronger oxidizing capacity located at the valence band maximum of WO_3 to participate in the photocatalytic reaction, thereby significantly improving the photocatalytic activity of the catalyst. With the further increase in WO_3 loading, when an excessive amount of WO_3 is added, agglomeration leads to an increase in carrier recombination centers and simultaneously blocks the active sites on the TiO_2 surface, resulting in a decrease in catalytic performance.

To further investigate the function of radicals underlying the photocatalytic reaction, quenching experiments were performed on TiO_2-5W. During the photocatalytic tests, specific scavengers were introduced into the reaction system to eliminate different active species: IPA for hydroxyl radicals (·OH), BQ for superoxide radicals ($\cdot O_2^-$), $AgNO_3$ for photogenerated electrons (e^-), and EDTA-2Na for photogenerated holes (h^+). The experimental results are presented in Figure 8a. It is clear that the addition of these radical scavengers significantly affects the catalytic performance of the TiO_2-5W sample. After 90 min of xenon lamp irradiation, the degradation rates of the systems containing $AgNO_3$, BQ, IPA, and EDTA-2Na are 89.5%, 75.2%, 57.9%, and 24.1%, respectively. These results reveal that quenching e^- (via $AgNO_3$ addition) exerted a negligible influence on the catalytic activity of TiO_2-5W, indicating that photogenerated e^- plays almost no role in the process of degradation. The addition of BQ led to a more significant decrease in photocatalytic efficiency compared to $AgNO_3$; this abnormal phenomenon can be explained by the fact that BQ competes with MB for holes or participates in hydroxyl radical-mediated degradation [51]. In contrast, the degradation efficiency of MB is drastically reduced in the systems in which h^+ are scavenged by EDTA-2Na and ·OH are eliminated by IPA. This demonstrates that photogenerated h^+ and their derived radicals are the primary active species responsible for methylene blue degradation, precisely because ·OH are further generated from photogenerated h^+, the effect of quenching h^+ is more significant.

Subsequently, electron paramagnetic resonance (EPR) tests are performed using DMPO as the spin-trapping agent to capture $\cdot O_2^-$ and ·OH, and using TEMPO to capture h^+

generated during photocatalysis. The results are shown in Figure 8b–d. From the spectrum in Figure 8b, it can be seen that persistent h^+ radicals exist in the system. The signal of h^+ is detectable even under dark conditions, which is due to the background signal of the trapping agent TEMPO itself. In addition, after turning on the xenon lamp, the intensity of the radical signal decreases slightly over time. With the onset of light irradiation, the peak height of the hole radicals decreases, since both h^+ and e^- radicals exhibit negative signals; thus, a decrease in peak height actually represents a further increase in radical concentration. This is consistent with the results of the quenching experiments. Light excitation activates TiO_2-5W, generating photogenerated electrons and holes, and h^+ plays a dominant role in the catalytic process. The EPR spectra for $\cdot O_2^-$ capture in Figure 8c show that no $\cdot O_2^-$ signal is detected in the dark, whereas a distinct signal emerged upon light irradiation and decreased in intensity with prolonged illumination time. This phenomenon is attributed to the synchronous generation of e^- alongside h^+ once the light source was switched on. Based on the band edge positions of TiO_2 and WO_3 in Figure 4, as well as the reaction potentials for the formation of superoxide radicals and hydroxyl radicals, it can be seen that electrons (e^-) in the conduction band minimum of TiO_2 possess the ability to reduce O_2 to superoxide radicals, while the holes (h^+) can further generate hydroxyl radicals. Therefore, these photo-generated electrons were subsequently converted into $\cdot O_2^-$ radicals with a shorter lifetime. Similar to the EPR spectra of $\cdot O_2^-$, Figure 8d displays the EPR spectra for ·OH capture. It is clear that no ·OH signal is observed without a light source, while a signal that decayed rapidly over time was detected under light irradiation, indicating that a fraction of h^+ was converted into a small amount of ·OH during the catalytic process. Owing to their high reactivity, ·OH radicals either participated in the reaction immediately or decayed rapidly after generation, resulting in a short lifetime. This also explains the phenomenon that the catalytic efficiency exhibited no significant decline in the quenching experiment with the addition of IPA.

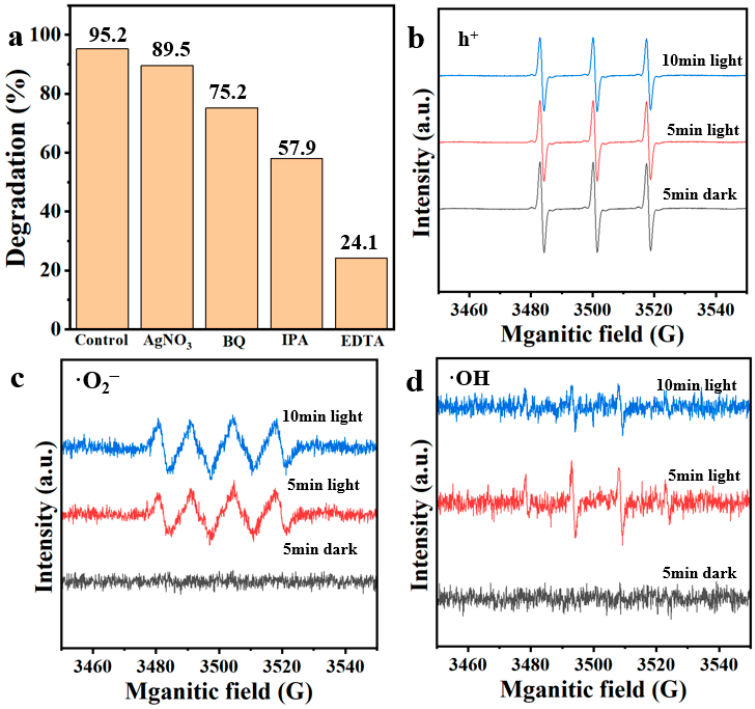


Figure 8. Quenching tests and EPR results of TiO_2-5W: (**a**) Quenching experiments; EPR spectra of DMPO-trapped radicals in aqueous dispersion under Xe lamp irradiation: (**b**) h^+, (**c**) $\cdot O_2^-$ and (**d**) ·OH.

Overall, h^+ is the most critical active species in the photocatalytic process of the TiO_2-5W heterojunction. Quenching of h^+ almost completely abrogated the photocatalytic activity of the composite, which can be ascribed to two key factors: Firstly, h^+ is the primary active species generated by the heterojunction. Secondly, ·OH is another important reactive radical which is further derived from h^+. These results are consistent with the previous analysis of the heterojunction band structure, namely that the construction of the S-scheme heterojunction facilitates charge carrier separation, and mitigates the recombination of the strongly oxidizing h^+ accumulated at the valence band of WO_3, thereby enabling more h^+ to participate in the photocatalytic reaction and ultimately enhancing the efficiency of methylene blue degradation by TiO_2.

3. Materials and Methods

3.1. Materials

Titanium tetrachloride ($TiCl_4$), Sodium tungstate dihydrate ($Na_2WO_4{\cdot}2H_2O$), Methylene blue (MB, $C_{16}H_{18}ClN_3S$), Hydrochloric acid (HCl, 36.5%), Silver nitrate ($AgNO_3$), Benzoquinone ($C_6H_4O_2$, BQ), Isopropyl alcohol (C_3H_8O, IPA), anhydrous copper sulfate ($CuSO_4$), Ethylene glycol ($C_2H_6O_2$, EG), and Disodium ethylenediaminetetraacetate ($C_{10}H_{14}N_2Na_2O_8$, EDTA-2Na) were of analytical reagent (AR) grade and purchased from Aladdin Co., Ltd., Shanghai, China. 5,5-Dimethyl-1-pyrroline N-oxide (DMPO) was purchased from Energy Chemical, Shanghai, China. $TiCl_4$, $C_2H_6O_2$, and HCl were used for the preparation of TiO_2 nanoflowers. $Na_2WO_4{\cdot}2H_2O$ was used for the preparation of the TiO_2/WO_3 heterojunction. MB was used to prepare the photocatalytic degradation solution.

3.2. Preparation of Samples

Preparation of TiO_2-0: Specifically, 2 mL of $TiCl_4$ was slowly added to 60 mL of ethylene glycol under continuous stirring. After the reaction was completed, 2 mL of $CuSO_4$ solution with a predetermined concentration was incorporated into the mixture (corresponding to a Cu mass fraction of 3% relative to TiO_2), followed by additional magnetic stirring for 2 h. Subsequently, the resulting mixture was transferred into an 80 mL Teflon-lined stainless-steel autoclave (Shanghai Shupei Experimental Equipment Co., Ltd., Shanghai, China) and subjected to hydrothermal treatment at 150 °C for 4 h. After natural cooling to room temperature, the product was collected by centrifugation and thoroughly rinsed with ethanol three times. The obtained precipitate was then dried overnight in an oven(DHG-9070A, Shanghai Yiheng Scientific Instrument Co., Ltd., Shanghai, China) at 60 °C, yielding the TiO_2-0 sample. Finally, the TiO_2-0 powder was calcined at 350 °C in ambient air for 4 h to obtain the sample labeled TiO_2, which was used as a reference sample, and calcined TiO_2-0 at 650 °C for 4 h to obtain the TiO_2-650 sample.

Preparation of TiO_2/WO_3 heterojunction (TiO_2-xW): First, 100 mg of the as-prepared TiO_2-0 powder was dispersed in 30 mL of deionized water via ultrasonic treatment to form a homogeneous suspension. A predetermined volume of 1 mg/mL $Na_2WO_4{\cdot}2H_2O$ aqueous solution was then added to the suspension, followed by magnetic stirring for 30 min to ensure uniform mixing. HCl was added dropwise to adjust the pH of the mixture to 2, and stirring was continued for another 2 h to ensure sufficient reaction. Subsequently, the mixture was centrifuged, and the collected precipitate was thoroughly rinsed with deionized water three times to remove unreacted impurities. The obtained precipitate was dried overnight in an oven at 60 °C. Finally, the dried sample was calcined in air at 350 °C for 4 h to fabricate the TiO_2/WO_3 heterojunction, denoted as TiO_2-xW in which x represents the mass percentage of $Na_2WO_4{\cdot}2H_2O$ relative to the initial TiO_2-0 powder.

Notably, all TiO_2-based samples (mainly anatase) in this work were Cu-doped TiO_2. The Cu doping is only part of the preparation procedure with the aim of modifying the TiO_2 matrix, and was not the focus of the present study.

3.3. Characterization

The crystal structure of the samples was characterized by X-ray diffraction (XRD, Rigaku SmartLab 9 kW, Rigaku Corporation, Tokyo, Japan). The elemental composition and chemical valence states were analyzed via X-ray photoelectron spectroscopy (XPS, Thermo Scientific Escalab 250Xi, Thermo Fisher Scientific, Waltham, MA, USA). The morphological features and microstructural details were observed using field emission scanning electron microscopy (FE-SEM Hitachi S-4800, Hitachi High-Technologies Corporation, Tokyo, Japan) and transmission electron microscopy (TEM, JEOL JEM-2100, JEOL Ltd., Tokyo, Japan). The specific surface area and pore size distribution were measured with a surface area and porosity analyzer (Micromeritics ASAP 2020, Micromeritics Instrument Corporation, Norcross, GA, USA). The electrochemical performance was evaluated on an electrochemical workstation (CH Instruments CHI660D, Shanghai Chenhua Instruments Co., Ltd., Shanghai, China). The optical absorption properties were tested using a UV-vis-nir spectrophotometer (Shimadzu UV-3600, Shimadzu Corporation, Kyoto, Japan) with approximately 100 mg of each sample. The electron paramagnetic resonance (ESR) spectra were recorded on an electron paramagnetic resonance spectrometer (Bruker EMX plus A300, Bruker Corporation, Billerica, MA, USA). The fluorescence spectra (PL) and time-resolved photoluminescence spectra (TR-PL) of the samples were recorded on an Edinburgh FLS 980 spectrometer (Edinburgh Instruments, Livingston, UK) using an excitation wavelength of 360 nm, to characterize the carrier separation efficiency. Time-resolved photoluminescence spectra were measured at an excitation wavelength of 375 nm, and the emission wavelength was 440 nm.

3.4. Photocatalytic Testing

A total of 10 mg of the as-prepared photocatalyst sample was uniformly dispersed in 50 mL of 10 mg/L methylene blue (MB) aqueous solution, and the initial PH was neutral. Prior to photocatalytic degradation, the suspension was subjected to dark adsorption for 1 h to achieve adsorption–desorption equilibrium. Subsequently, the photocatalytic degradation experiment was conducted under irradiation with a 300 W xenon lamp. At 10 min intervals, 3 mL aliquots of the reaction mixture were withdrawn. The collected aliquots were centrifuged, and the resulting supernatant was filtered through a mixed cellulose ester (MCE) membrane syringe filter to remove residual catalyst particles. The adsorption amount of MB was negligible. Finally, the absorbance of the clarified filtrate was measured at a characteristic wavelength of 661 nm using a UV-vis spectrophotometer (Shimadzu UV mini-1240, Shimadzu Corporation, Kyoto, Japan).

To evaluate the photocatalytic activity of the samples, photocatalytic degradation experiments of MB solution were conducted under irradiation from a xenon lamp source. According to the Lambert–Beer law, the absorbance was used to characterize the concentration of methylene blue in the solution. Further details regarding the photocatalytic reactor are provided in Figure S13.

For the quenching experiments, the TiO_2-5W sample was used, and all other conditions were kept identical to those in the photocatalytic experiments, except that excess quenchers were separately added during the reaction, including silver nitrate ($AgNO_3$), disodium ethylenediaminetetraacetate (EDTA-2Na), p-benzoquinone (BQ), and isopropanol (IPA).

3.5. Electrochemical Testing

A total of 10 mg of the as-prepared sample was uniformly dispersed in a mixed solvent consisting of 750 μL ethanol, 150 μL deionized water, and 100 μL Nafion solution(5 wt.%, D-520, The Chemours Company, Wilmington, DE, USA). The resultant homogeneous suspension was then uniformly coated onto a fluorine-doped tin oxide (FTO) conductive glass (Advanced Election Co., Ltd., Shanghai, China) substrate with an area of 1 cm^2 to form a thin film with consistent thickness. The coated substrate was dried overnight at 60 °C to improve the adhesion between the catalyst film and the FTO substrate.

Electrochemical measurements were carried out in a standard three-electrode electrochemical cell, using 0.2 mol/L Na_2SO_4 aqueous solution as the electrolyte. The working electrode (WE) was fabricated by clamping the FTO glass loaded with the photocatalyst film using a platinum clip (Leici, Shanghai INESA Scientific Instrument Co., Ltd., Shanghai, China). A saturated Ag/AgCl electrode (Leici, Shanghai INESA Scientific Instrument Co., Ltd., Shanghai, China) was employed as the reference electrode (RE), while a platinum sheet electrode (10 × 10 mm, purity ≥ 99.99%, Leici, Shanghai INESA Scientific Instrument Co., Ltd., Shanghai, China) served as the counter electrode (CE). The i-t curve measurements were performed using a 300 W xenon lamp (Beijing Perfectlight Technology Co., Ltd., Beijing, China) as the light source, with the three-electrode system positioned 10 cm away from the light source, no external bias voltage was applied during the test. Electrochemical impedance spectroscopy (EIS) measurements were performed on a CHI660D electrochemical workstation, with an alternating current (AC) amplitude of 5 mV and a frequency scanning range of 0.1 Hz to 10^6 Hz.

3.6. Theoretical Calculations

In this study, molecular dynamics (MD) calculations were performed using the Forcite module, with the parameters set as follows: The total simulation time was 100 ps, and the time step was 1 fs. The NPT ensemble was selected, and the temperature was set to 300 K. The Nose-Hoover thermostat was adopted for temperature control, and the force field was set to COMPASS III. In the "Dynamics" tab, the "Thermostat" was enabled, and the Velocity Verlet algorithm was used as the integration method. For non-bonded interactions, the atom-based summation method was employed, with a cutoff radius of 12.5 Å. The Ewald method was used for long-range electrostatic interactions, and the atom-based method with long-range correction was applied for van der Waals interactions. The initial velocities were randomly generated following the Maxwell–Boltzmann distribution. When calculating the thermal expansion coefficient of the model, the temperatures were set to 300 K and 500 K.

Based on the thermally equilibrated atomic configurations obtained from MD relaxation, first-principles density functional theory (DFT) calculations were performed to determine the work functions of TiO_2 and WO_3. All DFT computations were carried out using the $DMol^3$ module in Materials Studio. The generalized gradient approximation (GGA) with the Perdew–Burke–Ernzerhof (PBE) functional was adopted to describe the exchange-correlation interaction. A double numerical plus polarization (DNP) basis set was employed for all atoms, with a global orbital cutoff of 4.4 Å. The Brillouin zone was sampled using a Monkhorst–Pack k-point mesh of 3 × 3 × 1 for slab models of TiO_2 and WO_3. The convergence criteria were set as follows: energy tolerance of 1.0×10^{-5} Ha, maximum force tolerance of 0.002 Ha/Å, and maximum displacement tolerance of 0.005 Å. For work function calculations, slab models with a vacuum layer thickness of 20 Å were constructed to eliminate spurious periodic interactions along the surface normal direction. The work function was derived as the energy difference between the vacuum level and the Fermi level.

4. Conclusions

In conclusion, an S-scheme TiO_2-WO_3 heterojunction is successfully constructed via the in situ precipitation of WO_3 on TiO_2 surfaces in an aqueous system. Comprehensive structural and electronic characterizations confirmed the uniform deposition of WO_3 on TiO_2 without distinct interfacial transition layers, enabling efficient interfacial charge transfer. The difference in Fermi levels between TiO_2 and WO_3 induced interfacial charge redistribution and a built-in electric field directed from TiO_2 to WO_3, thereby establishing a typical S-scheme heterojunction. Benefiting from the enhanced charge separation and migration efficiency, the TiO_2-xWO_3 composite exhibited a significantly improved photocatalytic performance, especially TiO_2-5W, achieving over 95% degradation of methylene blue within 90 min under visible-light irradiation, which markedly surpassed that of pristine TiO_2 and WO_3. Radical trapping experiments further identified photogenerated h^+ and further generated ·OH from h^+ as the dominant active species in the photocatalytic process. These findings highlight the effectiveness of rational S-scheme heterojunction design in improving visible-light-driven photocatalysis, and provide valuable insights for the development of high-performance TiO_2-based photocatalysts for environmental remediation.

Supplementary Materials: The following supporting information can be downloaded at: https://www.mdpi.com/article/10.3390/catal16040342/s1. Figure S1: XRD result of TiO_2-0; Figure S2: SEM images of (a) TiO_2-0, (b) TiO_2, (c) TiO_2-650; Figure S3: FT-IR results of TiO_2-0, TiO_2 and TiO_2-650; Figure S4: (a,b) SEM images of TiO_2-0; (c,d) TEM and HRTEM images of TiO_2-0; Figure S5: (a,b) SEM images of TiO_2; (c,d) TEM and HRTEM images of TiO_2; Figure S6: XRD results of TiO_2 and TiO_2-5W; Figure S7: (a,b) SEM images of WO_3; (c,d) TEM images of WO_3; Figure S8: EDS-mapping results of TiO_2-5W; Figure S9: BET results of TiO_2 and TiO_2-5W; Figure S10: Tauc plots and band gaps of different samples; Figure S11: Structural models for electrostatic potential calculations of anatase TiO_2 (100) facet and WO_3 (100) facet; Figure S12: Photocatalytic performance of TiO_2-5W with different initial PH; Figure S13: Photograph of photocatalytic reactor(GHX-III photocatalytic reactor (Shanghai Jiapeng Technology Co., Ltd., Shanghai, China); Table S1: Detailed physical parameters of the prepared samples resulted from BET analysis; Table S2: Fitting parameters of TRPL results for TiO_2 and TiO_2-5W samples; Table S3: Summary of the photocatalytic performance of various material systems. Detailed characterization data and additional figures are provided in the Supplementary Materials [52–63].

Author Contributions: Y.D.: investigation, methodology, data curation, writing—original draft. S.W.: writing—review and editing, supervision. J.Z.: conceptualization, writing—review and editing, funding acquisition. All authors have read and agreed to the published version of the manuscript.

Funding: This research received no external funding.

Data Availability Statement: The data presented in this study are available on request from the corresponding author.

Acknowledgments: This project was supported by the National Research Foundation, Prime Minister's Office, Singapore, under its Campus for Research Excellence and Technological Enterprise (CREATE) program (CNSB).

Conflicts of Interest: The authors declare no conflict of interest.

References

1. Fujishima, A.; Honda, K. Electrochemical Photolysis of Water at a Semiconductor Electrode. *Nature* **1972**, *238*, 37–38. [CrossRef] [PubMed]
2. Armaković, S.J.; Savanović, M.M.; Armaković, S. Titanium Dioxide as the Most Used Photocatalyst for Water Purification: An Overview. *Catalysts* **2023**, *13*, 26. [CrossRef]
3. Hasham Firooz, M.; Naderi, A.; Moradi, M.; Kalantary, R.R. Enhanced tetracycline degradation with TiO_2/natural pyrite S-scheme photocatalyst. *Sci. Rep.* **2024**, *14*, 4954. [CrossRef] [PubMed]

4. Guo, Q.; Zhou, C.; Ma, Z.; Yang, X. Fundamentals of TiO_2 Photocatalysis: Concepts, Mechanisms, and Challenges. *Adv. Mater.* **2019**, *31*, e1901997. [CrossRef]
5. Liu, J.; Sun, X.; Fan, Y.; Yu, Y.; Li, Q.; Zhou, J.; Gu, H.; Shi, K.; Jiang, B. P–N Heterojunction Embedded CuS/TiO_2 Bifunctional Photocatalyst for Synchronous Hydrogen Production and Benzylamine Conversion. *Small* **2023**, *20*, e2306344. [CrossRef]
6. Abid, M.; Iatsunskyi, I.; Coy, E.; Lesage, G.; Ben Haj Amara, A.; Bechelany, M. Ag-BN/HNT-TiO_2 nanofibers produced by electrospinning as catalysts to remove acetaminophen. *Heliyon* **2024**, *10*, e24740. [CrossRef]
7. Zhou, L.; Shao, Y.; Yin, F.; Li, J.; Kang, F.; Lv, R. Stabilizing non-iridium active sites by non-stoichiometric oxide for acidic water oxidation at high current density. *Nat. Commun.* **2023**, *14*, 7644. [CrossRef]
8. Zu, D.; Ying, Y.; Wei, Q.; Xiong, P.; Ahmed, M.S.; Lin, Z.; Li, M.M.-J.; Li, M.; Xu, Z.; Chen, G.; et al. Oxygen Vacancies Trigger Rapid Charge Transport Channels at the Engineered Interface of S-Scheme Heterojunction for Boosting Photocatalytic Performance. *Angew. Chem. Int. Ed.* **2024**, *63*, e202405756. [CrossRef]
9. Li, F.; Liu, G.; Liu, F.; Wu, J.; Yang, S. Synergetic effect of CQD and oxygen vacancy to TiO_2 photocatalyst for boosting visible photocatalytic NO removal. *J. Hazard. Mater.* **2023**, *452*, 131237. [CrossRef]
10. Nagendraraj, T.; Noelson, E.A.; Soundarya, D.S.; Mani, I.; Ragavendran, V.; Mayandi, J.; Pandi, M.; Annaraj, J.; Sagadevan, S. Hybrid TiO_2-Ag_2O nanocomposites as efficient photocatalysts for the removal of medicinal pollutants in water under sunlight and study on their anticancer properties. *J. Alloys Compd.* **2024**, *982*, 173777. [CrossRef]
11. Zhang, B.; Sun, B.; Liu, F.; Gao, T.; Zhou, G. TiO_2-based S-scheme photocatalysts for solar energy conversion and environmental remediation. *Sci. China Mater.* **2024**, *67*, 424–443. [CrossRef]
12. Zhang, L.; Zhang, J.; Yu, J.; García, H. Charge-transfer dynamics in S-scheme photocatalyst. *Nat. Rev. Chem.* **2025**, *9*, 328–342. [CrossRef] [PubMed]
13. Low, J.; Yu, J.; Jaroniec, M.; Wageh, S.; Al-Ghamdi, A.A. Heterojunction Photocatalysts. *Adv. Mater.* **2017**, *29*, 1601694. [CrossRef] [PubMed]
14. Fu, J.; Xu, Q.; Low, J.; Jiang, C.; Yu, J. Ultrathin 2D/2D WO_3/g-C_3N_4 step-scheme H_2-production photocatalyst. *Appl. Catal. B Environ.* **2019**, *243*, 556–565. [CrossRef]
15. He, H.; Wang, Z.; Zhang, J.; Shao, C.; Dai, K.; Fan, K. Interface Chemical Bond Enhanced Ions Intercalated Carbon Nitride/CdSe-Diethylenetriamine S-Scheme Heterojunction for Photocatalytic H_2O_2 Synthesis in Pure Water. *Adv. Funct. Mater.* **2024**, *34*, 2315426. [CrossRef]
16. Gao, J.; Rao, S.; Yu, X.; Wang, L.; Xu, J.; Yang, J.; Liu, Q. Dimensional-matched two dimensional/two dimensional TiO_2/Bi_2O_3 step-scheme heterojunction for boosted photocatalytic performance of sterilization and water splitting. *J. Colloid Interface Sci.* **2022**, *628*, 166–178. [CrossRef]
17. Cui, H.; Cao, J.; Zhao, Y.; Wang, J.; Li, S.; Ge, K.; Chen, J.; Yang, Y. Construction of IO-B-TiO_2/In_2O_3 S-scheme heterojunction with photothermal effects and its highly efficient photocatalytic reduction of CO_2 under full-spectrum light. *Chem. Eng. J.* **2024**, *479*, 147618. [CrossRef]
18. Liapun, V.; Hanif, M.B.; Sihor, M.; Vislocka, X.; Pandiaraj, S.; Unnikrishnan, V.K.; Thirunavukkarasu, G.K.; Edelmannová, M.F.; Reli, M.; Monfort, O.; et al. Versatile application of $BiVO_4$/TiO_2 S-scheme photocatalyst: Photocatalytic CO_2 and Cr(VI) reduction. *Chemosphere* **2023**, *337*, 139397. [CrossRef]
19. Miranda, C.; Mansilla, H.; Yáñez, J.; Obregón, S.; Colón, G. Improved photocatalytic activity of g-C_3N_4/TiO_2 composites prepared by a simple impregnation method. *J. Photochem. Photobiol. A Chem.* **2013**, *253*, 16–21. [CrossRef]
20. Zhan, X.; Ding, C.; Zhao, Q.; Fang, Y. S-scheme TiO_2/Bi_2WO_6 heterojunction for enhanced photocatalytic selective oxidation of toluene. *Opt. Mater.* **2024**, *155*, 115860. [CrossRef]
21. Zhang, S.; Zhang, L.; Fang, S.; Zhou, J.; Fan, J.; Lv, K. Plasmonic semiconductor photocatalyst: Non-stoichiometric tungsten oxide. *Environ. Res.* **2021**, *199*, 111259. [CrossRef]
22. Vakarin, S.V.; Melyaeva, A.A.; Semerikova, O.L.; Kondratyuk, V.S.; Pankratov, A.A.; Plaksin, S.V.; Porotnikova, N.M.; Zaikov, Y.P.; Petrov, L.A.; Mikushina, Y.V.; et al. Catalase activity of coarse-grained and nanosized oxide tungsten bronzes obtained by electrolysis of molten salts. *Russ. Chem. Bull.* **2011**, *60*, 1985–1988. [CrossRef]
23. Huang, C.-W.; Zhou, S.-R.; Hsiao, W.-C. Multifunctional TiO_2/MIL-100(Fe) to conduct adsorption, photocatalytic, and heterogeneous photo-Fenton reactions for removing organic dyes. *J. Taiwan Inst. Chem. Eng.* **2024**, *158*, 104850. [CrossRef]
24. Chen, D.; Cheng, Y.; Zhou, N.; Chen, P.; Wang, Y.; Li, K.; Huo, S.; Cheng, P.; Peng, P.; Zhang, R.; et al. Photocatalytic degradation of organic pollutants using TiO_2-based photocatalysts: A review. *J. Clean. Prod.* **2020**, *268*, 121725. [CrossRef]
25. He, F.; Meng, A.; Cheng, B.; Ho, W.; Yu, J. Enhanced photocatalytic H_2-production activity of WO_3/TiO_2 step-scheme heterojunction by graphene modification. *Chin. J. Catal.* **2020**, *41*, 9–20. [CrossRef]
26. Zubkins, M.; Vibornijs, V.; Strods, E.; Aulika, I.; Zajakina, A.; Sarakovskis, A.; Kundziņš, K.; Korotkaja, K.; Rudevica, Z.; Letko, E.; et al. A stability study of transparent conducting WO_3/Cu/WO_3 coatings with antimicrobial properties. *Surf. Interfaces* **2023**, *41*, 103259. [CrossRef]

27. Zhao, M.; Liu, S.; Chen, D.; Zhang, S.; Carabineiro, S.A.C.; Lv, K. A novel S-scheme 3D $ZnIn_2S_4/WO_3$ heterostructure for improved hydrogen production under visible light irradiation. *Chin. J. Catal.* **2022**, *43*, 2615–2624. [CrossRef]
28. Leinekugel-le-Cocq-Errien, A.Y.; Deniard, P.; Jobic, S.; Gautier, E.; Evain, M.; Aubin, V.; Bart, F. Structural characterization of the hollandite host lattice for the confinement of radioactive cesium: Quantification of the amorphous phase taking into account the incommensurate modulated character of the crystallized part. *J. Solid State Chem.* **2007**, *180*, 322–330. [CrossRef]
29. Navidpour, A.H.; Abbasi, S.; Li, D.; Mojiri, A.; Zhou, J.L. Investigation of Advanced Oxidation Process in the Presence of TiO_2 Semiconductor as Photocatalyst: Property, Principle, Kinetic Analysis, and Photocatalytic Activity. *Catalysts* **2023**, *13*, 232. [CrossRef]
30. Zheng, T.; Sang, W.; He, Z.; Wei, Q.; Chen, B.; Li, H.; Cao, C.; Huang, R.; Yan, X.; Pan, B.; et al. Conductive Tungsten Oxide Nanosheets for Highly Efficient Hydrogen Evolution. *Nano Lett.* **2017**, *17*, 7968–7973. [CrossRef]
31. Van Der Voort, P.; Benjelloun, M.; Vansant, E.F. Rationalization of the Synthesis of SBA-16: Controlling the Micro- and Mesoporosity. *J. Phys. Chem. B* **2002**, *106*, 9027–9032. [CrossRef]
32. Cai, Z.; Bi, Y.; Hu, E.; Liu, W.; Dwarica, N.; Tian, Y.; Li, X.; Kuang, Y.; Li, Y.; Yang, X.-Q.; et al. Single-Crystalline Ultrathin Co_3O_4 Nanosheets with Massive Vacancy Defects for Enhanced Electrocatalysis. *Adv. Energy Mater.* **2018**, *8*, 1701694. [CrossRef]
33. Bao, J.; Zhang, X.; Fan, B.; Zhang, J.; Zhou, M.; Yang, W.; Hu, X.; Wang, H.; Pan, B.; Xie, Y. Ultrathin Spinel-Structured Nanosheets Rich in Oxygen Deficiencies for Enhanced Electrocatalytic Water Oxidation. *Angew. Chem. Int. Ed.* **2015**, *54*, 7399–7404. [CrossRef] [PubMed]
34. Ma, M.; Zhang, K.; Li, P.; Jung, M.S.; Jeong, M.J.; Park, J.H. Dual Oxygen and Tungsten Vacancies on a WO_3 Photoanode for Enhanced Water Oxidation. *Angew. Chem. Int. Ed.* **2016**, *55*, 11819–11823. [CrossRef]
35. Gomes, R.; de Sousa Pinheiro, G.; Serra, E.C.; Moreira, E.; Braga, S.D.; Azevedo, D.L.; Luz Lima, C.d. Theoretical and experimental study of the optoelectronic, thermodynamic and vibrational properties of the nanostructure of m-WO_3. *Ceram. Int.* **2024**, *50*, 8141–8149. [CrossRef]
36. Zuo, G.; Wang, Y.; Teo, W.L.; Xian, Q.; Zhao, Y. Direct Z-scheme TiO_2–$ZnIn_2S_4$ nanoflowers for cocatalyst-free photocatalytic water splitting. *Appl. Catal. B Environ.* **2021**, *291*, 120126. [CrossRef]
37. Niu, S.; Li, S.; Du, Y.; Han, X.; Xu, P. How to Reliably Report the Overpotential of an Electrocatalyst. *ACS Energy Lett.* **2020**, *5*, 1083–1087. [CrossRef]
38. Xu, Q.; Zhang, L.; Cheng, B.; Fan, J.; Yu, J. S-Scheme Heterojunction Photocatalyst. *Chem* **2020**, *6*, 1543–1559. [CrossRef]
39. Patel, M.Y.; Mortelliti, M.J.; Dempsey, J.L. A compendium and meta-analysis of flatband potentials for TiO_2, ZnO, and SnO_2 semiconductors in aqueous media. *Chem. Phys. Rev.* **2022**, *3*, 011303. [CrossRef]
40. Yang, H.G.; Sun, C.H.; Qiao, S.Z.; Zou, J.; Liu, G.; Smith, S.C.; Cheng, H.M.; Lu, G.Q. Anatase TiO_2 single crystals with a large percentage of reactive facets. *Nature* **2008**, *453*, 638–641. [CrossRef]
41. Ma, X.; Shi, Y.; Cheng, Z.; Liu, X.; Liu, J.; Guo, Z.; Cui, X.; Sun, X.; Zhao, J.; Tan, S.; et al. Unveiling diverse coordination-defined electronic structures of reconstructed anatase $TiO_2(001)$–(1×4) surface. *Nat. Commun.* **2024**, *15*, 2326. [CrossRef]
42. Kashiwaya, S.; Morasch, J.; Streibel, V.; Toupance, T.; Jaegermann, W.; Klein, A. The Work Function of TiO_2. *Surfaces* **2018**, *1*, 73–89. [CrossRef]
43. Zhang, X.; Ren, X.; Xiao, Z.; Huang, Y. Insight in the properties of WO_3 | Y: A first-principle study. *Results Phys.* **2019**, *15*, 102670. [CrossRef]
44. Zhang, G.; Li, X.; Chen, D.; Li, N.; Xu, Q.; Li, H.; Lu, J. Internal Electric Field and Adsorption Effect Synergistically Boost Carbon Dioxide Conversion on Cadmium Sulfide@Covalent Triazine Frameworks Core–Shell Photocatalyst. *Adv. Funct. Mater.* **2023**, *33*, 2308553. [CrossRef]
45. Zalouk, D.; Hatem, D.; Hocine, D.; Belkaid, M.S.; Hadjersi, T.; Kebbati, Y.; Boudinar, S. The influence of the mixed phase (Ti–TiO_2(A): TiO_2(R)) on the optical band gap of TiO_2 nanotubes heat treated at different temperatures. *J. Mater. Res.* **2023**, *38*, 3446–3457. [CrossRef]
46. Wang, Z.; Dong, C.; Tang, X.; Qin, X.; Liu, X.; Peng, M.; Xu, Y.; Song, C.; Zhang, J.; Liang, X.; et al. CO-tolerant RuNi/TiO_2 catalyst for the storage and purification of crude hydrogen. *Nat. Commun.* **2022**, *13*, 4404. [CrossRef]
47. Li, Y.; Feng, Y.; Bai, H.; Liu, J.; Hu, D.; Fan, J.; Shen, H. Enhanced visible-light photocatalytic performance of black TiO_2/SnO_2 nanoparticles. *J. Alloys Compd.* **2023**, *960*, 170672. [CrossRef]
48. Li, Y.; Cheng, D.; Wei, Z.; Sautet, P. Photoelectron Storage at the WO_3/TiO_2 Interface: Modeling in Ambient Conditions from First-Principles Calculations. *ACS Catal.* **2023**, *13*, 9979–9986. [CrossRef]
49. Malato, S.; Fernández-Ibáñez, P.; Maldonado, M.I.; Blanco, J.; Gernjak, W. Decontamination and disinfection of water by solar photocatalysis: Recent overview and trends. *Catal. Today* **2009**, *147*, 1–59. [CrossRef]
50. Ambika, S.; Devasena, M.; Nambi, I.M. Single-step removal of Hexavalent chromium and phenol using meso zerovalent iron. *Chemosphere* **2020**, *248*, 125912. [CrossRef]
51. Puga, F.; Navío, J.A.; Hidalgo, M.C. A critical view about use of scavengers for reactive species in heterogeneous photocatalysis. *Appl. Catal. A Gen.* **2024**, *685*, 119879. [CrossRef]

52. Djellabi, R.; Yang, B.; Adeel Sharif, H.M.; Zhang, J.; Ali, J.; Zhao, X. Sustainable and easy recoverable magnetic TiO_2-Lignocellulosic Biomass@Fe_3O_4 for solar photocatalytic water remediation. *J. Clean. Prod.* **2019**, *233*, 841–847. [CrossRef]
53. Safardoust-Hojaghan, H.; Salavati-Niasari, M. Degradation of methylene blue as a pollutant with N-doped graphene quantum dot/titanium dioxide nanocomposite. *J. Clean. Prod.* **2017**, *148*, 31–36. [CrossRef]
54. Konstantinou, I.K.; Sakellarides, T.M.; Sakkas, V.A.; Albanis, T.A. Photocatalytic degradation of selected s-triazine herbicides and organophosphorus insecticides over aqueous TiO_2 suspensions. *Environ. Sci. Technol.* **2001**, *35*, 398–405. [CrossRef]
55. ChongYeon, P.; Ghosh, T.; ZeDa, M.; Kefayat, U.; Vikram, N.; WonChun, O. Preparation of CuS-graphene oxide/TiO_2 composites designed for high photonic effect and photocatalytic activity under visible light. *Chin. J. Catal.* **2013**, *34*, 711–717.
56. Jiang, L.; Gao, X.; Chen, S.; Ashok, J.; Kawi, S. Oxygen-Deficient WO_3/TiO_2/CC Nanorod Arrays for Visible-Light Photocatalytic Degradation of Methylene Blue. *Catalysts* **2021**, *11*, 1349. [CrossRef]
57. Dai, Z.; Ren, P.; Cao, Q.; Gao, X.; He, W.; Xiao, Y.; Jin, Y.; Ren, F. Synthesis of TiO_2@lignin based carbon nanofibers composite materials with highly efficient photocatalytic to methylene blue dye. *J. Polym. Res.* **2020**, *27*, 108. [CrossRef]
58. Cai, J.; Hu, S.; Xiang, J.; Zhang, H.; Men, D. The effect of graphitized carbon on the adsorption and photocatalytic degradation of methylene blue over TiO_2/C composites. *RSC Adv.* **2020**, *10*, 40830–40842. [CrossRef]
59. Liu, Z.; Zhang, F.; Li, C.; Inoue, C. Enhanced Visible Light Response and Characterization of Nanoscale TiO_2/WO_{3-x} Composite Photocatalyst by Sol–gel Synthesis. *Catal. Lett.* **2023**, *153*, 2936–2949. [CrossRef]
60. Du, Q.; Lin, Y.; Cheng, S.; Wei, D.; Wang, Y.; Zhou, Y. In situ synthesis of three-dimensional flower-like TiO_2/WO_3 heterojunction: Enhanced visible photocatalytic properties and theoretical calculations. *Ceram. Int.* **2024**, *50*, 30605–30616. [CrossRef]
61. Feng, X.; Li, X.; Su, B.; Ma, J. Two-step construction of WO_3@TiO_2/CS-biochar S-scheme heterojunction and its synergic adsorption/photocatalytic removal performance for organic dye and antibiotic. *Diam. Relat. Mater.* **2023**, *131*, 109560. [CrossRef]
62. Ibrahim, Y.O.; Gondal, M.A. Visible-light-driven photocatalytic performance of a Z-scheme based TiO_2/WO_3/g-C_3N_4 ternary heterojunctions. *Mol. Catal.* **2021**, *505*, 111494. [CrossRef]
63. Sangchay, W. WO_3-Doped TiO_2 Coating on Charcoal Activated with Increase Photocatalytic and Antibacterial Properties Synthesized by Microwave-Assisted Sol-Gel Method. *J. Nanotechnol.* **2017**, *2017*, 7902930. [CrossRef]

Disclaimer/Publisher's Note: The statements, opinions and data contained in all publications are solely those of the individual author(s) and contributor(s) and not of MDPI and/or the editor(s). MDPI and/or the editor(s) disclaim responsibility for any injury to people or property resulting from any ideas, methods, instructions or products referred to in the content.